Untangling the effects of octahedral rotation and ionic displacements on the electronic structure of $BiFeO_3$

Iflah Laraib,* Marciano A. Carneiro, and Anderson Janotti†
Department of Materials Science and Engineering, University of Delaware, Newark, Delaware 19711, USA

(Received 8 April 2021; revised 10 June 2021; accepted 21 July 2021; published 29 July 2021)

The electronic structure and related properties of perovskites ABO_3 are strongly affected by even small modifications in their crystalline structure. In the case of $BiFeO_3$, variations in the octahedral rotations and ionic displacements lead to significant changes in the band gap. This effect can possibly explain the wide range of values (2.5–3.1 eV) reported in the literature, obtained from samples of varied structural qualities, including polycrystalline films, epitaxial films grown by pulsed-laser deposition and molecular beam epitaxy, nanowires, nanotubes, and bulk single crystals. Using hybrid density-functional calculations, we investigate the dependence of the electronic structure on the crystal lattice distortions of the ferroelectric-antiferromagnetic $BiFeO_3$, disentangling the effects of the ferroelectric ionic displacements and the antiferrodistortive octahedral rotations on the band gap and the band-edge positions. The band gap is shown to vary from 3.39 eV for the rhombohedral ground-state (*R3c*) structure down to 1.58 eV for the perfect cubic ($Pm\bar{3}m$) structure, with changes in the conduction band being much more prominent than in the valence band. The gap varies linearly with the ferroelectric ionic displacements, but nonlinearly with the octahedral rotations around the pseudocubic $[111]_c$ axis, and this is explained in terms of the different interactions between Bi 6*s*, 6*p*, Fe 3*d*, and O 2*p* bands. We argue that such large variation of the band gap with structural changes may well explain the large scattering of the reported values, especially if significant deviations from the equilibrium crystal structure are found near domain boundaries, extended defects, or grain boundaries in polycrystalline films.

DOI: 10.1103/PhysRevB.104.035159

I. INTRODUCTION

Multiferroics are materials that combine magnetism and ferroelectricity; they are potentially important for memory and other electronic devices due to the possibility of coupled control of magnetic and ferroelectric ordering through the magnetoelectric effect [1]. $BiFeO_3$ is one of the rare examples of multiferroic materials, being ferroelectric and antiferromagnetic [2,3]. At room temperature, the ground-state rhombohedral crystal structure of $BiFeO_3$, *R3c* space group, has been described as a combination of (i) antiferrodistortive counter-rotations of the FeO_6 octahedra around the body diagonal of the five-atom primitive cubic cell (pseudocubic $[111]_c$ axis) and (ii) displacement of Fe and O atoms along the same pseudocubic $[111]_c$ axis [2,4], as shown in Fig. 1(a). $BiFeO_3$ displays a G-type antiferromagnetic ordering with cycloid spiral canting of the magnetic moment over 620 Å [5] and a Néel temperature of 623 K; it becomes paraelectric, with rhombohedral $R\bar{3}c$ structure [Fig. 1(b)], at a much higher Curie temperature of about 1100 K, and transforms to cubic structure, $Pm\bar{3}m$ space group [Fig. 1(c)], at 1200 K [6–8].

Varying ferroelectric and magnetic properties along with other crystal structures have also been reported in the literature on $BiFeO_3$. Early work showed the presence of weak ferroelectric polarization in single crystals with the rhombohedral *R3c* structure [9]. Later, strong ferroelectric polarization was reported in epitaxially grown thin films with monoclinic structures [10,11]. More recently, thin films of tetragonal symmetry were reported to exhibit nanoscale switching, yet again indicating strong ferroelectric properties albeit in a different symmetry [12]. In other reports on crystals of $BiFeO_3$ with *R3c* structure, epitaxial strain has been shown to have little effect on polarization strength [13,14]. Reports on the effects of the different crystal structures and strain conditions on the electronic structure have been scarce [15].

The band gap of $BiFeO_3$ has been determined by several experimental groups, yet its value remains a subject of debate, varying over a wide range from 2.5 to 3.1 eV. Thin films of rhombohedral $BiFeO_3$ grown by molecular beam epitaxy were shown to exhibit a band gap of 2.74 eV [16], while films grown by pulsed laser deposition [17–19] have shown band gaps in the range of 2.67 eV to 2.82 eV. $BiFeO_3$ bulk crystals on the other hand, exhibit a band gap of 2.5 eV according to one report [6] and 3.1 eV per another [20].

Predictions of the band gap of $BiFeO_3$ based on first-principles calculations have also shown large variation, depending on the details of the method employed. Using spin density functional theory (DFT) within the local density approximation with an additional electron-electron interaction U for the Fe d orbitals (LSDA+U, $U = 4$ eV), Neaton *et al.* [4] predicted a band gap of 1.9 eV for *R3c* $BiFeO_3$. Later, Clark and Robertson [21] obtained a band gap of 2.8 eV using the screened exchange (sX) functional and suggested that a similar value could be obtained using $U = 5$-6 eV in the DFT+U

*laraib@udel.edu
†janotti@udel.edu

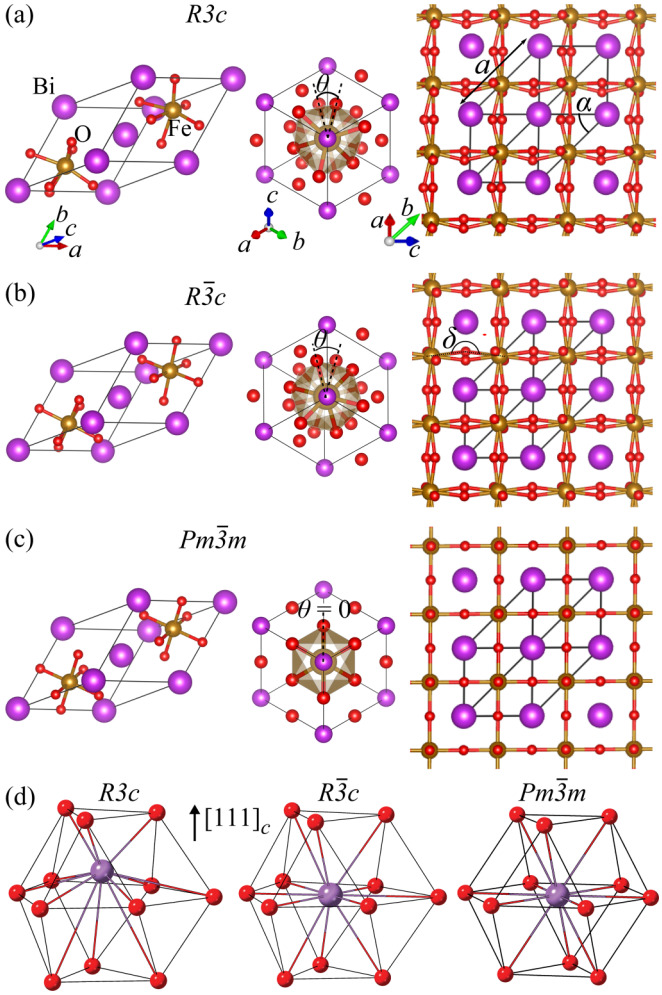

FIG. 1. Ball and stick model representing the unit cell, lattice parameters (a and α) along with Fe–O–Fe angle (δ) and O–Fe Fe–O dihedral angle (θ) for the three phases of $BiFeO_3$: (a) ground-state rhombohedral $R3c$, (b) paraelectric rhomboheral $R\bar{3}c$, and (c) perfect cubic $Pm\bar{3}m$. The 12 nearest-neighbor O atoms to each Bi are shown in (d) for the $R3c$, $R\bar{3}c$, and $Pm\bar{3}m$ phases.

approach. More recently, a band gap of 2.58 eV was reported using DFT+U, with $U = 5$ eV [22]. Using the screened hybrid functional HSE06, with 25% Hartree-Fock mixing, Stroppa and Picozzi [23] predicted a band gap of 3.4 eV for $R3c$ $BiFeO_3$. Quasiparticle G_0W_0 calculations based on the wave functions from HSE06 predicted a band gap of 3.8 eV, while including vertex corrections led to a gap of 3.3 eV. These later results (HSE06 and G_0W_0 with vertex corrections) are in reasonably good agreement with the experimental value of 3.1 eV based on absorption and photoluminescence spectra of single crystals [20], and raise the question of whether the much lower values from other previous experiments are related to defects or to deviations in the crystal structure (i.e., octahedral rotations and/or ionic displacements) due to different strain conditions found in thin films and nanostructures. Thus, a systematic study of the relationship between the details of the crystal structure and band gap of $BiFeO_3$ might shed light on the wide range of reported values.

In this paper, we present a detailed first-principles study of the relationship between the crystal structure and electronic properties of $BiFeO_3$, untangling the effects of FeO_6 octahedral rotations and the Fe/O ionic displacements on the band gap and band-edge positions. We track the evolution of the electronic structure, starting from the ground-state $R3c$ phase, by first reversing the Fe/O ionic displacements from the ferroelectric $R3c$ to the paraelectric $R\bar{3}c$ phase, and then reversing the FeO_6 octahedral rotation from the paraelectric $R\bar{3}c$ to the perfect cubic phase of $BiFeO_3$, $Pm\bar{3}m$ space group. We discuss the effects of these structural transformations on the electronic structure, including the low-lying Bi 6s bands, the empty Bi 6p bands, the spin-split Fe 3d bands, the band gap, and the positions of the valence-band maximum (VBM) and conduction-band minimum (CBM).

II. COMPUTATIONAL DETAILS

The calculations are based on spin-polarized DFT [24,25] and the screened hybrid functional of Heyd, Scuseria, and Enzerhof with 25% Hartree Fock mixing (HSE06) [26,27] as implemented in the VASP code [28,29]. Projector augmented wave potentials are used to describe the interaction between the valence electrons and the ionic cores [30]. An energy cutoff of 600 eV is used for the plane wave basis set, and forces on each atom are minimized until they are less than 0.01 eV/Å. All the calculations were performed using rhombohedral unit cells containing two formula units, as shown in Fig. 1, so we can easily compare the transformations between the $R3c$, $R\bar{3}c$, and perfect cubic $Pm\bar{3}m$ phase of $BiFeO_3$. A $4\times4\times4$ mesh of special k-points was employed for the integrations over the Brillouin zone. Density of states calculations were performed using a finer $12\times12\times12$ Γ-centered k-point mesh.

Intermediate structures between the ferroelectric ground-state $R3c$ and the paraelectric $R\bar{3}c$ phase, and between $R\bar{3}c$ and the $Pm\bar{3}m$ phase were generated by a simple interpolation between the two end structures, for which we determined band gaps and band-edge positions. In these calculations, we constrained the volumes of the $R\bar{3}c$ and $Pm\bar{3}m$ structures to be the same as that of the $R3c$ structure. In this way, we can directly compare the band-edge positions of the intermediate and endpoint configurations, since they have the same average electrostatic (Hartree) potential and, therefore, the same reference for the single-particle energy eigenvalues. We also kept the antiferromagnetic ordering in all calculations, allowing us to focus on the effects of structural variations on the electronic structure.

III. RESULTS AND DISCUSSION

A. Structural parameters of $BiFeO_3$

The calculated equilibrium structural parameters of $BiFeO_3$ in the ground-state antiferromagnetic ferroelectric $R3c$ phase are listed in Table I. The lattice parameters a of 5.641 Å and angle α of 59.11° between the lattice vectors are in good agreement with the experimental values of 5.634 Å and 59.35° [31]. Each Fe atom is bonded to six oxygen atoms, forming FeO_6 octahedra that are distorted (i.e., deviate from perfect octahedra) due to Fe/O ferroelectric displacements, resulting in two sets of Fe–O distances, and Fe–O–Fe angle

TABLE I. Lattice parameters, atomic positions, lattice distortion angles, and band gap (E_g) of $BiFeO_3$ as reported experimentally for *R3c* phase [31] and obtained by HSE06 calculations, along with those of $R\bar{3}c$ and $Pm\bar{3}m$ phase structures modeled for this study.

Material/ property	*R3c* Exp.	*R3c*	$R\bar{3}c$	$Pm\bar{3}m$
a (Å)	5.634	5.641	5.641	5.603
α (°)	59.35	59.11	59.11	60
V (Å^3)	124.60	124.39	124.39	124.39
x_{Fe}	0.221	0.220	0.250	0.250
x_O	0.443	0.433	0.500	0.500
y_O	0.019	0.027	0.064	0.000
z_O	0.952	0.892	0.936	0.000
δ (°)	154.1	153.6	159.6	180
E_g (eV)	2.5–3.10	3.39	2.82	1.58

$\delta = 153.6°$ connecting two octahedra (in the perfect cubic $Pm\bar{3}m$ phase, $\delta = 180°$). The two octahedra in the rhombohedral unit cell are counter rotated around the pseudocubic $[111]_c$ axis, with a dihedral O–Fe Fe–O angle θ of 25.02°. The calculated equilibrium volume of 124.39 Å^3 for the ten-atom unit cell is only slightly lower than the value of 124.60 Å^3 obtained from the experimental values for lattice parameters a and α.

The $Pm\bar{3}m$ structure is an ideal perovskite where the Fe atom is at fractional coordinates (0.25,0.25,0.25) and (0.75,0.75,0.75). The FeO_6 octahedra align atop each other along the pseudocubic $[111]_c$ axis (see Fig. 1) and are highly symmetric with equal Fe–O bond lengths and O–Fe–O angle of 180°. The $R\bar{3}c$ phase is characterized by counter rotations of the two FeO_6 octahedra around the $[111]_c$ axis, without displacing the Fe atoms. Such rotation leads to a nonzero dihedral angle O–Fe Fe–O (of 25.02° in our case) and a reduction of the $Pm\bar{3}m$ symmetry.

The arrangement of O atoms around the Bi atoms, shown in Fig. 1(d), is of great importance to the discussion of the electronic structure of $BiFeO_3$, as will be demonstrated in later sections of the paper. In the perfect cubic $Pm\bar{3}m$ phase, each Bi has 12 nearest-neighbor O atoms, forming a cuboctahedron, with six O atoms in the plane perpendicular to $[111]_c$, forming a hexagon with Bi at the center, and three atoms in the plane below and three atoms in the plane above, forming the triangular base of the cuboctahedron. In this case, the Bi–O distances are all equal to 2.802 Å. In the $R\bar{3}c$ phase, where only octahedral rotations are considered, the hexagon is distorted, maintaining equal sides (same O–O distances) and Bi is at the center of mass, with three shorter Bi–O distances of 2.426 Å and three longer Bi–O distances of 3.140 Å. The distances between the Bi and O atoms located in the planes above and below are all equal to 2.843 Å. In the ground-state *R3c* phase, the O/Fe atoms are displaced such that the Bi atom gets displaced out of the distorted hexagonal plane, and the distances between the Bi and the O atoms located in the plane above become 2.262 Å, and in the plane below become 3.469 Å. In the distorted hexagon, we find three shorter Bi–O distances of 2.505 Å and three longer Bi–O distances of 3.233 Å. Considering the Bi–O bond distances in the various phases of Bi_2O_3, from 2.1 Å to 2.6 Å [32], we find that in *R3c*-$BiFeO_3$, the Bi strongly interacts with six O atoms (three at 2.262 Å and three at 2.505 Å). In the $R\bar{3}c$ phase, Bi strongly interacts with only three in-plane O atoms at 2.426 Å. In the $Pm\bar{3}m$ phase, the Bi atom only weakly interacts with the 12 O atoms at 2.802 Å.

The transformation of *R3c*-$BiFeO_3$ into the $R\bar{3}c$ and $Pm\bar{3}m$ phases, in practice, is accompanied by changes in volume [7]. However, we model the $R\bar{3}c$ and $Pm\bar{3}m$ unit cells maintaining the same volume (and number of formula units) as that of the optimized *R3c* unit cell, and keeping the antiferromagnetic ordering in all the calculations, as discussed above. Doing so enables us to eliminate the effects of volume change and magnetic ordering, and focus on the antiferrodistortive rotation and ferroelectric displacement alone. For completeness, we also calculated $BiFeO_3$ in the relaxed $R\bar{3}c$ and $Pm\bar{3}m$ phases for comparison. We find that the ground state *R3c* phase is lower in energy by 0.614 eV/f.u. than the $R\bar{3}c$ phase, and by 1.298 eV/f.u. than the $Pm\bar{3}m$ phase. We also find that volume slightly contracts as we go from the *R3c* to the relaxed $R\bar{3}c$ and $Pm\bar{3}m$ phases, in agreement with previous calculations [7]. The calculated band gaps of relaxed $R\bar{3}c$ and $Pm\bar{3}m$ slightly change compared to the respective phases constrained to the equilibrium volume of the *R3c* phase, by less than 0.05 eV, indicating that the volume effect in our analysis can indeed be neglected. Note that previous calculations [13] have shown that the effect of strain on the spontaneous ferroelectric polarization in *R3c* $BiFeO_3$ thin films is also negligible, indicating weak coupling between volume changes and ferroelectric polarization.

B. Electronic band structure and magnetic ordering of $BiFeO_3$

The electronic band structure of $BiFeO_3$ in the *R3c*, $R\bar{3}c$, and $Pm\bar{3}m$ phases, are shown in Fig. 2, plotted along a k-path defined in the Brillouin zone of the 10-atom rhombohedral unit cell. Note that only the antiferromagnetic ordering has been considered here. First, for the ground-state *R3c* $BiFeO_3$, we predict a direct band gap of 3.39 eV (with both VBM and CBM at the Z point) which is close to values of 3.05–3.10 eV reported by Moubah *et al.* based on absorption and photoluminescence spectra of high-quality bulk single *R3c* $BiFeO_3$ crystals [20]. Our results are also in agreement with previous calculations using HSE06 and G_0W_0 with vertex corrections [23]. For the $R\bar{3}c$ phase, we find a direct band gap of 2.82 eV, also at Z, but lower than that of the *R3c* phase. Others have also reported that the band gap of the $R\bar{3}c$ is lower than that of the *R3c* phase [7]. Finally, for the $Pm\bar{3}m$ phase, we obtain an indirect gap of 1.58 eV, with the VBM at Z and CBM at F in the Brillouin zone of the rhombohedral unit cell. The magnetic moments on the two Fe atoms remain basically unchanged (yet opposite in sign) through the structural transformation, being 4.12 μ_B for the *R3c*, 4.13 μ_B for the $R\bar{3}c$, and 4.12 μ_B for the $Pm\bar{3}m$ phase. These values are obtained by projecting the occupied bands on spherical harmonics inside a sphere of radius 1.302 Å around each Fe atom. Thus, our results indicate a high-spin configuration for the Fe atoms (d^5) for the three phases.

Previously, the $Pm\bar{3}m$ phase has been reported at high temperatures, between 920°C and 933°C [6,8], and reported to be

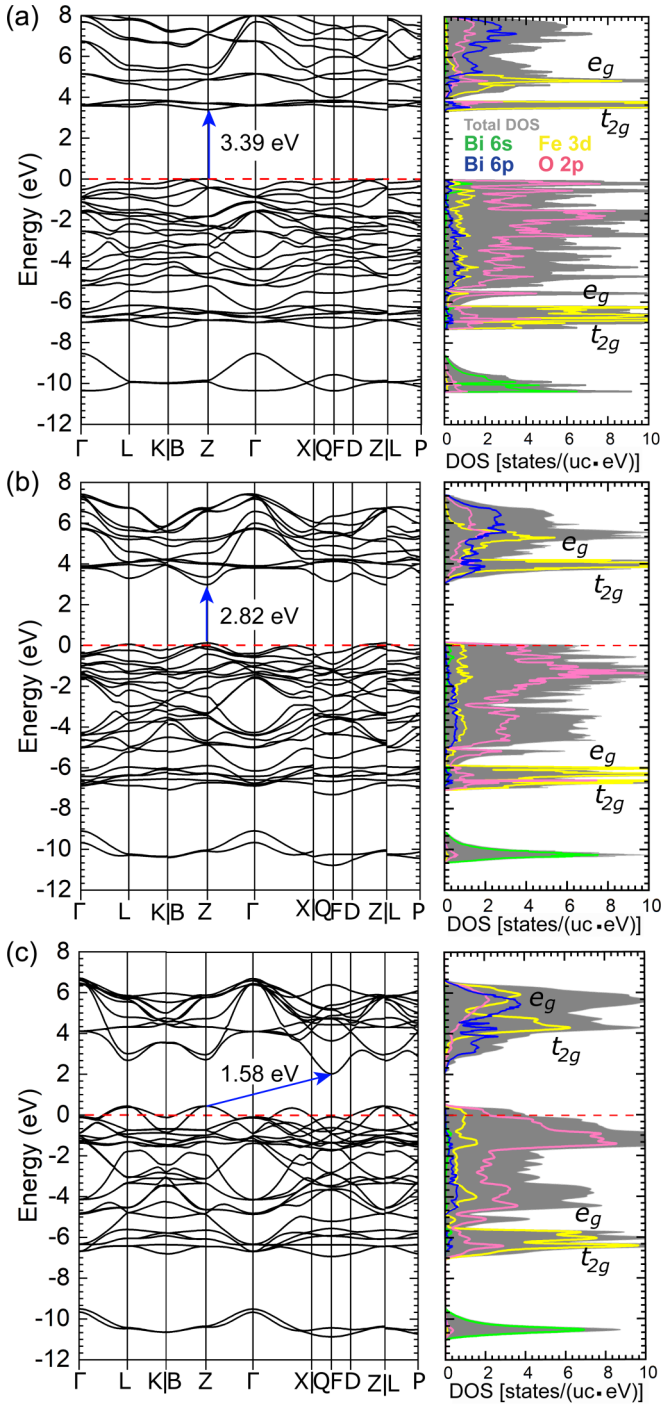

FIG. 2. Band structure and total density of states (DOS, in units of states per unit cell per eV) along with its projection on Bi 6s, Bi 6p, Fe 3d, and O 2p orbitals for (a) $R3c$, (b) $R\bar{3}c$, and (c) $Pm\bar{3}m$ phase $BiFeO_3$. The VBM of $R\bar{3}c$ and $Pm\bar{3}m$ phases are higher than that of the ground-state $R3c$ phase, used as reference and indicated by the dashed line in each plot. The arrows indicate the fundamental band gap. The VBM of the $R\bar{3}c$ and $Pm\bar{3}m$ phases are 0.14 and 0.46 eV higher than that of the $R3c$ phase. The location of the Fe 3d t_{2g} and e_g bands are also indicated, identified as described in the text.

metallic. However, this occurs at temperatures where $BiFeO_3$ is nonmagnetic. In fact, nonmagnetic calculations of $Pm\bar{3}m$ $BiFeO_3$ do give a zero gap, metallic solution. In contrast, we find that $Pm\bar{3}m$ $BiFeO_3$ with antiferromagetic ordering has a band gap of 1.58 eV.

From the orbital-resolved density of states (DOS), also shown in Fig. 2, we note some important characteristics and differences between the three phases. First, and most notable, the CBM has a sizable contribution from Bi 6p in the $R3c$ phase, and this contribution becomes predominant in the $R\bar{3}c$ and $Pm\bar{3}m$ phases. Second, the occupied Fe 3d bands are located well below the VBM, between −6 eV and −7 eV, yet contributions from Fe 3d are also found through the upper part of the valence band due to the interaction with the O 2p bands. This, in particular, is in good agreement with soft x-ray emission spectroscopy measurements of Higuchi *et al.* [33]. Third, the unoccupied Fe 3d bands greatly contribute to the CBM in the $R3c$ phase and are slightly higher than the CBM in the $R\bar{3}c$ and $Pm\bar{3}m$ phases. The three t_{2g} and two e_g bands are identified by inspecting the partial charge density at Γ of each occupied band. The t_{2g} bands have lobes pointing to directions between the Fe–O bonds, forming π bonds, whereas the e_g bands have lobes pointing along the Fe–O bonds, forming stronger direct covalent bonds. Their location with respect to the band edges is indicated in the DOS plots of Fig. 2 and schematically represented in Fig. 3(a), where the contributions from each Fe to each spin channel are indicated. Finally, the Bi 6s bands are located at ∼ −10 eV below the VBM.

The bands near the VBM are composed of O 2p, Bi 6s, Fe 3d, and Bi 6p (in decreasing order) in the $R3c$ phase; of O 2p, Fe 3d, and Bi 6s in $R\bar{3}c$; and of O 2p and Fe 3d in the $Pm\bar{3}m$ phase. The most relevant interactions that impact the CBM, VBM, and thus the gap, are illustrated in Fig. 3. As seen in the DOS plots, the Fe 3d bands become wider, going from $R3c$ to $R\bar{3}c$, as the octahedra become regular (equal Fe–O bond length), and from $R\bar{3}c$ to $Pm\bar{3}m$, as the Fe–O–Fe form 180° angles with increased Fe 3d and O 2p orbital overlap.

In the $R3c$ phase, the bands near the VBM and CBM are quite narrow. The bands near the VBM become broader in the $R\bar{3}c$ phase, with increased interaction with the Fe 3d, pushing the VBM upward by 0.14 eV. The CBM moves downward by 0.43 eV from the $R3c$ to the $R\bar{3}c$ phase. The largest contribution being from the Bi 6p, the bands near the CBM in the $R\bar{3}c$ are much more dispersed with significant increase in width. This is attributed to a decrease in the interaction between the Bi 6p and O 2p bands, lowering the former, due to the O atoms being more symmetrically distributed around the Bi atoms and with larger Bi–O distances in the $R\bar{3}c$ phase than in $R3c$. This effect also causes a decrease of the Bi 6s contribution to the VBM, reducing the band width of the Bi 6s bands near −10 eV.

Finally, in the $Pm\bar{3}m$ phase, the VBM is pushed up by 0.32 eV (with respect to that in $R\bar{3}c$), largely due to the increased Fe 3d and O 2p overlap in the $Pm\bar{3}m$ structure, leading to a significant increase in the dispersion of bands near the VBM. The CBM is pushed down by 0.92 eV due to a decrease in the interaction between the Bi 6p and O 2p bands, as the three shorter Bi–O distances of 2.426 Å in the $R\bar{3}c$ increase and all the Bi–O distances become equal to 2.802 Å in the $Pm\bar{3}m$ phase.

Note that the Bi 6s contribution to the top of the valence band decreases going from the $R3c$ to $R\bar{3}c$ and to the $Pm\bar{3}m$

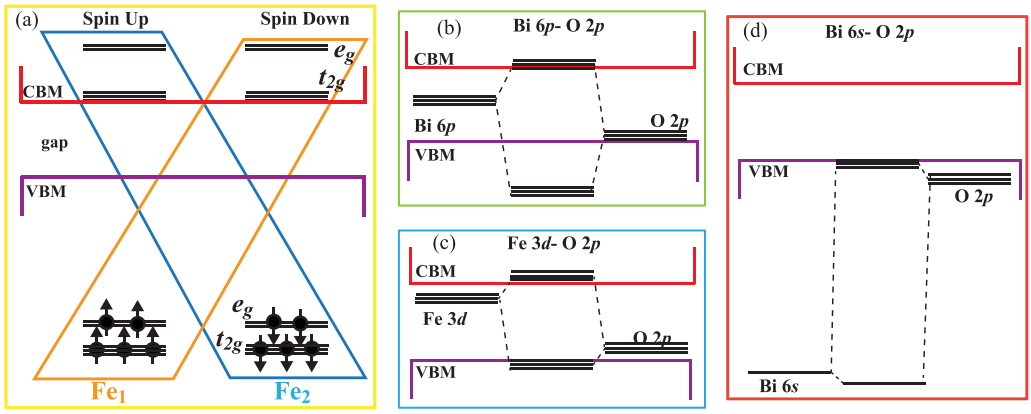

FIG. 3. Orbital interactions that affect the band gap and position of the band edges VBM and CBM in $R3c$-$BiFeO_3$. (a) Positions of the Fe $3d$ t_{2g} and e_g bands showing the contribution of the t_{2g} bands to the CBM. The occupation shows the high-spin configuration of each of the Fe atoms in the unit cell, and their contributions to the occupied and unoccupied $3d$ bands in each spin are specified. (b) Interaction between the Bi $6p$ and O $2p$ that impacts the CBM. (c) Interaction between the unoccupied Fe $3d$ (t_{2g}) and O $2p$ that pushes down the VBM. (d) Interaction between the Bi $6s$ and O $2p$ that pushes up the VBM.

phase, accompanied by a decrease in bandwidth of the occupied lower lying Bi $6s$ band at -10 eV. It is interesting to note that the width of the Bi $6s$ band decreases as the symmetry of the lattice increases, an effect that at first seems counterintuitive. However, it has to be noted that due to the ionic displacements of the ferroelectric $R3c$ phase, a subset of the neighboring O atoms move closer to the Bi atoms, while the other O atoms move away, increasing/decreasing the overlap between Bi $6s$ and O $2p$, resulting in one wider and the other narrower band centered at -10 eV, as shown in Fig. 2(a).

C. Effects of FeO_6 octahedral rotations and Fe/O ionic displacements on the band gap of $BiFeO_3$

Here we determine how the band gap and band edges of $BiFeO_3$ vary as the structure transforms from $R3c$, to $R\bar{3}c$, and to $Pm\bar{3}m$, disentangling the effects of ferroelectric ionic displacements and octahedral rotations. Starting with the ten-atom unit cell of the ferroelectric $R3c$ phase, first we undo the ferroelectric ionic displacements, bringing the distorted FeO_6 octahedra, with Fe-O distances of 1.95 Å ($\times 3$) and 2.12 ($\times 3$) Å to regular octahedra with equal Fe-O distances of 2.01 Å, keeping the antiferrodistosive rotation of the paraelectric $R\bar{3}c$ phase. We generate four intermediate configurations by averaging the atomic positions of the $R3c$ and $R\bar{3}c$ phases, keeping the lattice vectors and angle α unchanged. This ensures that the volume remains unchanged and that the average electrostatic potential, which is used as a reference for the single-particle energies, remains constant. The variation of the band gap, VBM, and CBM are shown on the left side of Fig. 4. The band gap decreases almost linearly from 3.39 eV to 2.82 eV, from $R3c$ to $R\bar{3}c$, as the Fe and O atoms are displaced to their centrosymmetric positions in the regular FeO_6 octahedra. The largest change occurs at the CBM, which linearly decreases by 0.43 eV, while the VBM linearly increases by only 0.14 eV.

The linear change of the CBM with the ferroelectric ionic displacements in $BiFeO_3$ is attributed to the sole effect of decreasing the Bi $6p$ and O $2p$ interaction [Fig. 3(b)], going from the $R3c$ with shortest Bi–O distances of 2.262 Å between the Bi and the O atoms in the upper basal plane of the cuboctahedron to 2.843 Åin the $R\bar{3}c$ phase [Fig. 1(d)]. The O $2p$ bands that interact with the Bi $6p$ are located near the middle of the valence band as seen from the projections of the Bi $6p$ orbitals, and thus, do not affect the valence band. The VBM is only slightly affected by the ionic displacements. We attribute this to two competing effects: (i) the interaction between the unoccupied Fe $3d$ t_{2g} and O $2p$ [Fig. 3(c)], forming π bonds that compose the VBM, broadening the bands and raising the VBM as the Fe–O–Fe angle (δ in Table I) increases from 153.6° to 159.6°; (ii) the repulsion between the low-lying Bi $6s$ band and the O $2p$ bands [Fig. 3(d)] that decreases from the $R3c$ to the $R\bar{3}c$ phase, decreasing the VBM. Both effects are small (relatively small change in δ and large energy difference between the Bi $6s$ and the O $2p$ near the VBM) yet the former dominates, leading to a slight increase in the VBM.

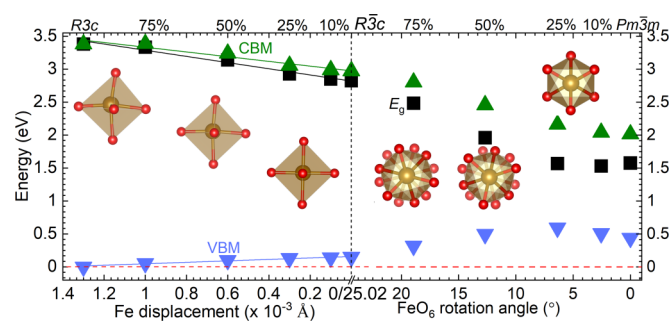

FIG. 4. Variations in the band gap, valence-band maximum (VBM), and conduction-band minimum (CBM) with respect to structural modifications in $BiFeO_3$, going from the ground-state $R3c$, to $R\bar{3}c$, and to the $Pm\bar{3}m$ phase. The left side shows variation in gap, VBM, and CBM when Fe and O ions are displaced, transforming the ferroelectric $R3c$ into the paraelectric $R\bar{3}c$ phase. The right side shows variation in gap, VBM, and CBM when FeO_6 octahedra are rotated back to 0° O–Fe Fe–O angle through which the $R\bar{3}c$ phase is transformed into the $Pm\bar{3}m$ phase. These structural transformations are represented in the ball & stick models in the inset.

From the $R\bar{3}c$ to $Pm\bar{3}m$ phase, we again generate four intermediate configurations corresponding to 75, 50, 25, and 10% rotation of the FeO_6 octahedra, where we interpolated both atomic positions and lattice vectors, reaching a=5.603 Å and $\alpha = 60^\circ$. Here, the antiferrodistorsive rotation of the FeO_6 octahedra in the $R\bar{3}c$ phase, characterized by a O–Fe Fe–O dihedral angle θ=25.02°, is undone, bringing θ to zero in the $Pm\bar{3}m$ phase. The largest effect, again, is on the CBM, which varies almost linearly, and we attribute it to the decreasing repulsion between the Bi 6p and O 2p bands in the middle of the valence band going from the $R\bar{3}c$ to the perfect cubic $Pm\bar{3}m$ phase. The shortest Bi–O distances of 2.426 Å between the Bi and three O in the plane of the distorted hexagon in the $R\bar{3}c$ phase [Fig. 1(d)] increase, and all the Bi–O distances become equal to 2.802 Å, forming a perfect cuboctahedron, in the $Pm\bar{3}m$ phase.

The VBM, on the other hand, slowly increases, then reaches a maximum shift of 0.51 eV for θ=6.4°, and finally decreases to 0.46 eV for θ, with respect to the VBM of the original $R3c$ structure. This behavior is also attributed to a competition between the coupling of the unoccupied Fe 3d t_{2g} and O 2p and the repulsion of the Bi 6s and O 2p bands. The coupling between the unoccupied Fe 3d t_{2g} and O 2p has two effects: it pushes the VBM down as the repulsion between these two bands is stronger in the $Pm\bar{3}m$ phase in which their overlap is maximized, widening the bonding/antibonding distance of the π bonds; second, it pushes the VBM up by the broadening of bands that compose it due to the increased overlap between the Fe 3d t_{2g} and O 2p orbitals as θ approaches zero and δ approaches 180°, and this can be clearly seen by comparing Figs. 2(b) and 2(c). Additionally, a third effect, the repulsion between the Bi 6s and O 2p, pushes the VBM down, going from $R\bar{3}c$ to $Pm\bar{3}m$, as the shortest Bi–O distances increase from 2.426 Å to being all equal to 2.802 Å in the $Pm\bar{3}m$ phase. These combined effects result in a nonlinear variation of VBM and the band gap with the octahedral rotation, starting from 2.82 eV ($R\bar{3}c$) to 1.57 eV for $\theta =\sim 6^\circ$, and then slightly increases to 1.58 eV for $\theta = 0^\circ$ due to the lowering of the VBM.

The discussion above regarding the role of the Bi 6p on the CBM also leads us to address the nature of the Bi lone pair in $BiFeO_3$. It is often argued that the lone pair comes from a coupling between the occupied low lying Bi 6s with the O 2p making up the top of the valence band in the $R3c$ phase [34,35]. Such coupling would be the driving force for the observed ferroelectric ordering as well. However, from the discussion above and the results shown in Figs. 2 and 3, it is clear that the coupling between the unoccupied Bi 6p and the O 2p bands in the middle of the valence band are much stronger, lifting the Bi 6p band by almost 1.4 eV as the octahedral rotations and ionic displacements are combined to give the structure of the $R3c$ phase. In contrast, the coupling between the Bi 6s with the O 2p bands barely changes the center of gravity of the former despite a change in dispersion which is noticeable on comparing Figs. 2(a) and 2(c). Therefore, we argue that the coupling between the unoccupied 6p with the O 2p is the dominant effect leading to the lone pair in $BiFeO_3$.

Considering these large variations of band gap with octahedral rotations and ionic displacements, as shown in Fig. 4, it is reasonable to state that the large scattering in the reported values for the band gap of $BiFeO_3$ may well be related to the variations in strain conditions. In thin films and nanostructures, lower values for band gap are often observed, and in single crystals where the lattice is fully relaxed and of high structural quality, higher values are reported. We also note that a correlation between octahedral rotation and band gap in $BiFeO_3$ has been reported in studies of the ferroelectric domain walls, whose local structure is characterized by a decrease in octahedral rotation, leading to decreased band gap and increased conductivity [36].

IV. SUMMARY

We find a band gap of 3.39 eV for the ground-state $R3c$ $BiFeO_3$, that is, higher than the often quoted values in the literature (2.5–3.1 eV). It is, however, in reasonable agreement with the value of 3.1 eV from photoluminescence spectroscopy measurements on crystals of high structural quality. Our calculations for the band gap as a function of structural variations, from the ground-state $R3c$ to the paraelectric $R\bar{3}c$ and to the perfect cubic perovskite structures show large dependence on Fe/O ferroelectric displacements and FeO_6 octahedral rotations, with the largest effect being on the conduction band. The CBM varies almost linearly with the ferroelectric ionic displacements (from $R3c$ to $R\bar{3}c$) and also with the octahedral rotations (from $R\bar{3}c$ to $Pm\bar{3}m$) due to the strong coupling between the empty Bi 6p and occupied O 2p bands. The VBM varies much slower, but nonlinearly, due to competing effects of the coupling between the Fe 3d t_{2g} and O 2p and between the low-lying Bi 6s and O 2p. The combination of these effects explains the linear variation of the band gap with ionic displacements and nonlinear behavior with the FeO_6 octahedral rotations. These results suggest that the wide range of reported band gaps of $R3c$ $BiFeO_3$ can be attributed to small variations in the structure caused by strain, extended defects or domain walls. The present paper points to the need for further studies on single crystals of high structural quality for precise determination of the structural, electronic, and optical properties of this material.

ACKNOWLEDGMENTS

This work was supported by the NSF Early Career Award Grant No. DMR-1652994, the Extreme Science and Engineering Discovery Environment (XSEDE) supported by National Science Foundation Grant No. ACI-1053575, and the Information Technologies (IT) resources at the University of Delaware.

[1] M. Fiebig, J. Phys. D: Appl. Phys. **38**, R123 (2005).
[2] N. A. Hill, Annu. Rev. Mater. Res. **32**, 1 (2002).
[3] N. A. Spaldin and R. Ramesh, Nat. Mater. **18**, 203 (2019).

[4] J. B. Neaton, C. Ederer, U. V. Waghmare, N. A. Spaldin, and K. M. Rabe, Phys. Rev. B **71**, 014113 (2005).

[5] I. Sosnowska, T. P. Neumaier, and E. Steichele, J. Phys. C: Solid State Phys. **15**, 4835 (1982).

[6] R. Palai, R. S. Katiyar, H. Schmid, P. Tissot, S. J. Clark, J. Robertson, S. A. T. Redfern, G. Catalan, and J. F. Scott, Phys. Rev. B **77**, 014110 (2008).

[7] S. M. Selbach, T. Tybell, M. A. Einarsrud, and T. Grande, Adv. Mater. **20**, 3692 (2008).

[8] S. A. T. Redfern, J. N. Walsh, S. M. Clark, G. Catalan, and J. F. Scott, arXiv:0901.3748.

[9] J. R. Teague, R. Gerson, and W. J. James, Solid State Commun. **8**, 1073 (1970).

[10] J. Wang, J. B. Neaton, H. Zheng, V. Nagarajan, S. B. Ogale, B. Liu, D. Viehland, V. Vaithyanathan, D. G. Schlom, U. V. Waghmare, N. A. Spaldin, K. M. Rabe, M. Wuttig, and R. Ramesh, Science **299**, 1719 (2003).

[11] H. Béa, M. Bibes, S. Petit, J. Kreisel, and A. Barthélémy, Philos. Mag. Lett. **87**, 165 (2007).

[12] D. Mazumdar, V. Shelke, M. Iliev, S. Jesse, A. Kumar, S. V. Kalinin, A. P. Baddorf, and A. Gupta, Nano Lett. **10**, 2555 (2010).

[13] C. Ederer and N. A. Spaldin, Phys. Rev. Lett. **95**, 257601 (2005).

[14] C. Ederer and N. A. Spaldin, Phys. Rev. B **71**, 224103 (2005).

[15] S. Jethva, S. Katba, M. Bhatnagar, M. Ranjan, D. Shukla, and D. G. Kuberkar, J. Appl. Phys. **125**, 082510 (2019).

[16] J. F. Ihlefeld, N. J. Podraza, Z. K. Liu, R. C. Rai, X. Xu, T. Heeg, Y. B. Chen, J. Li, R. W. Collins, J. L. Musfeldt, X. Q. Pan, J. Schubert, R. Ramesh, and D. G. Schlom, Appl. Phys. Lett. **92**, 142908 (2008).

[17] S. R. Basu, L. W. Martin, Y. H. Chu, M. Gajek, R. Ramesh, R. C. Rai, X. Xu, and J. L. Musfeldt, Appl. Phys. Lett. **92**, 091905 (2008).

[18] D. Sando, C. Carrétéro, M. N. Grisolia, A. Barthélémy, V. Nagarajan, and M. Bibes, Adv. Opt. Mater. **6**, 1700836 (2018).

[19] J. Xu, R. Zhang, Z. Chen, Z. Wang, F. Zhang, X. Yu, A. Jiang, Y. Zheng, S. Wang, and L. Chen, Nanoscale Res. Lett. **9**, 188 (2014).

[20] R. Moubah, G. Schmerber, O. Rousseau, D. Colson, and M. Viret, Appl. Phys. Express **5**, 183502 (2012).

[21] S. J. Clark and J. Robertson, Appl. Phys. Lett. **90**, 132903 (2007).

[22] S. M. Young, F. Zheng, and A. M. Rappe, Phys. Rev. Lett. **109**, 236601 (2012).

[23] A. Stroppa and S. Picozzi, Phys. Chem. Chem. Phys. **12**, 5405 (2010).

[24] W. Kohn and L. J. Sham, Phys. Rev. **140**, A1133 (1965).

[25] P. Hohenberg and W. Kohn, Phys. Rev. **136**, B864 (1964).

[26] J. Heyd, G. E. Scuseria, and M. Ernzerhof, J. Chem. Phys. **118**, 8207 (2003).

[27] A. V. Krukau, O. A. Vydrov, A. F. Izmaylov, and G. E. Scuseria, J. Chem. Phys. **125**, 224106 (2006).

[28] G. Kresse and J. Hafner, Phys. Rev. B **47**, 558 (1993).

[29] G. Kresse and J. Hafner, Phys. Rev. B **49**, 14251 (1994).

[30] P. E. Blöchl, Phys. Rev. B **50**, 17953 (1994).

[31] F. Kubel and H. Schmid, Acta Cryst. B **46**, 698 (1990).

[32] A. Matsumoto, Y. Koyama, and I. Tanaka, Phys. Rev. B **81**, 094117 (2010).

[33] T. Higuchi, Y.-S. Liu, P. Yao, P.-A. Glans, J. Guo, C. Chang, Z. Wu, W. Sakamoto, N. Itoh, T. Shimura, T. Yogo, and T. Hattori, Phys. Rev. B **78**, 085106 (2008).

[34] R. Seshadri and N. A. Hill, Chem. Mater. **13**, 2892 (2001).

[35] A. Walsh, D. J. Payne, R. G. Egdell, and G. W. Watson, Chem. Soc. Rev. **40**, 4455 (2011).

[36] J. Seidel, L. W. Martin, Q. He, Q. Zhan, Y. H. Chu, A. Rother, M. E. Hawkridge, P. Maksymovych, P. Yu, M. Gajek, N. Balke, S. V. Kalinin, S. Gemming, F. Wang, G. Catalan, J. F. Scott, N. A. Spaldin, J. Orenstein, and R. Ramesh, Nat. Mater. **8**, 229 (2009).